DOI: 10.1111/cgf.70138
Eurographics Conference on Visualization (EuroVis) 2025
W. Aigner, N. Andrienko, and B. Wang
(Guest Editors)

COMPUTER GRAPHICS *forum*
Volume 44 (2025), Number 3

Fast HARDI Uncertainty Quantification and Visualization with Spherical Sampling

Tark Patel[1], Tushar M. Athawale[2], Timbwaoga A. J. Ouermi[1], and Chris R. Johnson[1]

[1]Scientific Computing and Imaging Institute, University of Utah, US
[2]Oak Ridge National Lab, Tennessee, US

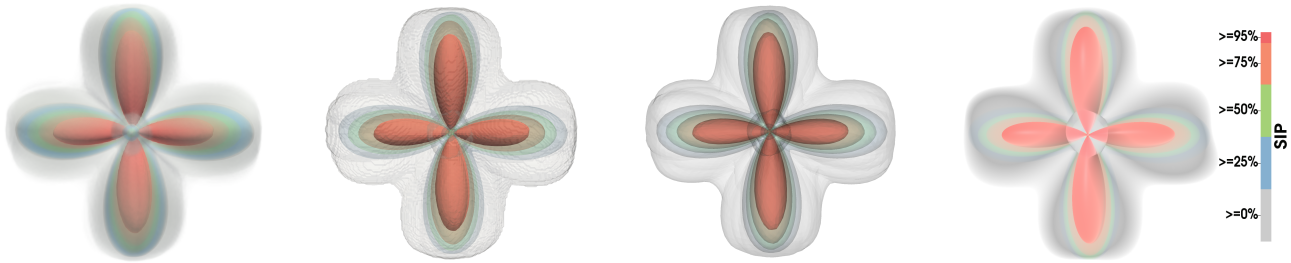

(a) *Volume-sampled SIP function (32MB, ∼12 min. computation) illustrated in Figure 4c.*

(b) *Isosurfaces of volume-sampled SIP function (200KB, ∼12 min. computation) illustrated in Figure 4d.*

(c) *Spherically-sampled isosurfaces of SIP function (125KB, ∼5.8 sec. computation) illustrated in Figure 5e.*

(d) *Volume representation of spherically-sampled SIP function (900B, ∼85 ms. computation) illustrated in Figure 5f.*

Figure 1: *Our spherical sampling method (c & d) shows improved accuracy while significantly reducing computational runtime and memory requirements for uncertainty visualization of HARDI glyphs compared to the existing state-of-the-art volume sampling method (a & b) [JPGJ12]. The isosurfaces of the shape inclusion probability (SIP) function are rendered with different colors and transparency to depict confidence intervals representing positional and orientation uncertainty of HARDI glyphs. In particular, the innermost opaque red isosurface represents the high-confidence positions, and the translucent outermost gray isosurface denotes low-confidence positions.*

Abstract

In this paper, we study uncertainty quantification and visualization of orientation distribution functions (ODF), which corresponds to the diffusion profile of high angular resolution diffusion imaging (HARDI) data. The shape inclusion probability (SIP) function is the state-of-the-art method for capturing the uncertainty of ODF ensembles. The current method of computing the SIP function with a volumetric basis exhibits high computational and memory costs, which can be a bottleneck to integrating uncertainty into HARDI visualization techniques and tools. We propose a novel spherical sampling framework for faster computation of the SIP function with lower memory usage and increased accuracy. In particular, we propose direct extraction of SIP isosurfaces, which represent confidence intervals indicating spatial uncertainty of HARDI glyphs, by performing spherical sampling of ODFs. Our spherical sampling approach requires much less sampling than the state-of-the-art volume sampling method, thus providing significantly enhanced performance, scalability, and the ability to perform implicit ray tracing. Our experiments demonstrate that the SIP isosurfaces extracted with our spherical sampling approach can achieve up to 8164× speedup, 37282× memory reduction, and 50.2% less SIP isosurface error compared to the classical volume sampling approach. We demonstrate the efficacy of our methods through experiments on synthetic and human-brain HARDI datasets.

CCS Concepts

• ***Human-centered computing*** → ***Scientific visualization;*** • ***Computing methodologies*** → ***Uncertainty quantification;*** *Ray tracing;* • ***Mathematics of computing*** → ***Probabilistic algorithms; Bootstrapping;***

1. Introduction

Diffusion-weighted imaging (DWI) is a magnetic resonance imaging (MRI) technique for measuring water diffusion in fibrous tis-

sue, such as muscle and nerve cells. Fibrous tissue has anisotropic diffusion, which can be measured along a set of gradient vectors. Diffusion is measured by acquiring multiple DWI scans, each with a gradient vector along which diffusion is measured. We refer to an ensemble of 3D DWI scans as a DWI volume.

Diffusion imaging techniques typically construct approximate models per-voxel based on ensembles of diffusion-weighted images. Many models have been developed in the pursuit of creating a compact representation to design efficient visualization algorithms [ODWL19]. Diffusion tensor imaging (DTI) is a popular method for modeling diffusion with tensors, which are 3x3 symmetric matrices [BML94]. The DTI model can represent single fiber directions, but it fails to accurately capture multiple fiber populations with varying orientations, such as fiber crossings. High angular resolution diffusion imaging (HARDI) modeling methods overcome the limitation of a single prominent diffusion assumption [TRW*02]. HARDI methods typically construct orientation distribution functions (ODFs) of the diffusion or fiber orientation profiles. Though HARDI requires more scans, it can still be performed in a clinically feasible time [TCGC04].

Quantifying and visualizing uncertainty has been regarded as the top scientific challenge to mitigate data misrepresentation [Joh04, JS03, BOL12]. Because model fitting provides a best-fit estimate of the underlying DWI data, models discard the residual, which is the modeling error. Because residuals are influenced by noise, they provide insight into how well the model fits the measured signal. Bootstrapping is commonly used to investigate model uncertainty by generating samples based on residuals [CLH06, Jon08].

The shape inclusion probability (SIP) function is a state-of-the-art mathematical tool to capture and visualize the variation of an ensemble of ODFs or tensors, such as those generated from bootstrapping. We discuss SIP functions in more detail in Section 3.4. Jiao et al. [JPGJ12] compute the SIP function with a 3D structured grid, which we call the *volume sampling method* [JPGJ12]. We refer to the sampling grid as the sampling volume. A glyph is visualized by volume rendering the measured SIP function per voxel.

Volume sampling has significant limitations concerning the performance and memory footprint for quantification and visualization. The computation of the SIP function exhibits quartic time computational complexity, $O(R^3N)$, where R is the sampling volume's resolution and N number of bootstrap simulations. This sampling volume is costly to store on disk and in memory. The SIP functions are typically visualized with volume rendering, which is limited by available memory. These limitations impede the integration of SIP function analysis into HARDI visualization tools and necessitate investigating more efficient sampling methods.

This manuscript has been authored by UT-Battelle, LLC under Contract No. DE-AC05-00OR22725 with the U.S. Department of Energy. The publisher, by accepting the article for publication, acknowledges that the U.S. Government retains a non-exclusive, paid up, irrevocable, world-wide license to publish or reproduce the published form of the manuscript, or allow others to do so, for U.S. Government purposes. The DOE will provide public access to these results in accordance with the DOE Public Access Plan (http://energy.gov/downloads/doe-public-access-plan).

To address volume sampling's storage and computational limitations, we propose *spherical sampling*, a novel method for computing the SIP distribution function with a spherical basis. Sampling exhibits cubic time complexity $O(\Theta^2 N)$ with a sorting cost of $O(\Theta^2 N \log N)$, where Θ is the polar and azimuthal resolution and N is the number of bootstrap samples. In addition to the significant improvement in computation time, spherical sampling converges faster and has a smaller memory footprint than volume sampling. Additionally, we propose a novel upsampling method, which reduces sampling requirements and memory footprint.

We propose another novel visualization method of volume rendering glyphs with implicit ray tracing, which enables continuous and data-efficient rendering without tessellation. Recent work by Peter et al. proposed an uncertainty glyph method. However, they lacked a method to construct real datasets [PPUJ23]. Our volumetric ray tracing glyphs are rendered using their framework.

Our contributions are summarized below.

- We propose a fast, accurate, and memory-efficient method for evaluating ODF model uncertainty by computing the SIP function with spherical sampling.
- We extend the framework of ODF modeling to SIP isosurfaces, which provides a compact and continuous representation of the SIP isosurfaces that are efficiently tessellated and rendered.
- For SIP isosurfaces modeling with a spherical harmonics (SH) basis, we introduce an implicit uncertainty glyph with multiple volumes. Implicit ray tracing renders smooth, continuous surfaces without tessellation and has little memory overhead.

2. Related Work

Many HARDI ODF models have developed in pursuit of an expressive and compact basis [MD13, TRW*02, MVYM06, Fra02, TCGC04, MRS10, MR10, BVF08]. The ability of HARDI methods to distinguish multiple fiber populations has aided in the detection of pathologies, such as vision impairment [BHK*14, BHZ*17], immaturity at birth [TCR*13], and Alzheimer's Disease [HRC*11]. Visualization methods typically visualize ODFs or tensors directly as glyphs or derive prominent fiber pathways. Glyph visualization is useful for validating tractography because tracking bias is avoided. Unlike standard DTI glyphs [BML94, Kin04], HARDI glyphs can disambiguate fiber crossings because the underlying models are of sufficient complexity, such as the SH basis, described in Section 3.2. Rendering of HARDI glyphs is typically performed by deforming spherical meshes [PPvA*09] or implicitly ray tracing primitives [PPUJ23, vAPP*11].

Tractography visualization methods [BPP*00, WSSS14] show likely fiber pathways by tracing streamlines through the dataset based on model-estimated fiber directions and user-defined tracking parameters [BPP*00, BHK*14]. In addition to model error, tractography has an additional error because directions and endpoints of fiber pathways are estimations [Cal19]. Tractography uncertainty visualization methods mitigate fiber pathway error by statistically analyzing streamline ensembles [BPtHRV13, SHV21, SVBK13, OVVDW10, ESM*05, CZCE08, MMB*09, SG24]. However, tractography-based methods do not directly convey model uncertainty [JJ11]. Though bootstrapping has been used with tractog-

raphy uncertainty visualization methods, model uncertainty is obscured by the streamline tracking algorithm [CADW11]. Additionally, fiber tracking is influenced by user-defined parameters, which heavily influence resulting tracts [PWP*15, HRC*11].

Several glyph visualization methods analyzed individual components of model uncertainty [Jon03, AWHS16, ZCH*17, ZSL*16, SSSSW13]. Some visualization methods intuitively show uncertainty with an opaque glyph encompassed by a transparent glyph, representing high and low probabilities [TCGC04, TCC07, GRT19]. Though these methods are elegant for DTI tensors, there is no extension to HARDI data, which is better suited for the disambiguation of fiber crossings. Jiao et al. introduced an ODF uncertainty glyph with various volumetric intervals [JPGJ12]. They render intervals from the Shape Inclusion Probability(SIP) [LP08] function using volume rendering, which is inefficient concerning both time and memory. We propose a novel sampling strategy and data format to improve performance, memory usage, and accuracy.

Recent work by Peter et al. introduced an uncertainty glyph that renders an opaque glyph encompassed by one volumetric interval using implicit ray tracing of spherical harmonics [PPUJ23]. Their uncertainty rendering technique is promising. However, they state that there is no existing method to compute real uncertainty data for their method. We propose modeling SIP interval boundaries, which can utilize Peter et al.'s uncertainty glyph. Additionally, we extend their method to visualize multiple volume intervals, similar to Jiao et al.'s method [JPGJ12].

3. Background

This section covers the process of quantifying ODF uncertainty for SIP functions [JPGJ12], which is illustrated in Figure 2. Per-voxel ODF models are estimated and represented in the spherical harmonics basis. Bootstrapping is applied to generate an ensemble of models that convey residual-based uncertainty. Then, the shape inclusion probability function is estimated from the bootstrap ensemble.

3.1. Model Fitting

Modeling is a form of approximation with a set of continuous, parametric basis functions, which is illustrated in Figure 2b. Figure 2a shows the discrete ODF, which is mapped to a basis. The mapping is defined as $K(S) = A$ where the DWI signal $S = [S_1, S_2, \ldots, S_G]$, basis function coefficients $A = [A_1, A_2, \ldots, A_{j_{max}}]$, and j_{max} is the total number of coefficients. Because the SIP function is model-agnostic [JPGJ12], any spherical ODF model

$$\Psi(\vec{V}, A) = \sum_{j=0}^{j_{max}} A_j P_j(\vec{V}) \tag{1}$$

is defined as a summation of basis functions P_j, where $j \in [1, \ldots, j_{max}]$, for any given vector $\vec{V} = [\theta, \phi]$ where $\theta \in [0, \pi]$ and $\phi \in [0, 2\pi]$. Any solution of Ψ must be unique, such that the ODF shape has no holes. We define a corresponding inversion $K^{-1}(A) = \hat{S}$ as the model-based diffusion signal prediction $\hat{S} = [\hat{S}_1, \hat{S}_2, \ldots, \hat{S}_G]$.

Within the HARDI framework, there are multiple techniques to model the orientation distribution functions (ODFs). Though spherical sampling works for any ODF, we utilize fiber orientation distribution functions (fODFs) derived from constrained spherical deconvolution (CSD) in our experiments. CSD derives the fODF by deconvolving a diffusion orientation distribution function (dODF) [ALS*10] with a response kernel and uses a positivity constraint because negative fibers are physically impossible [TCC07].

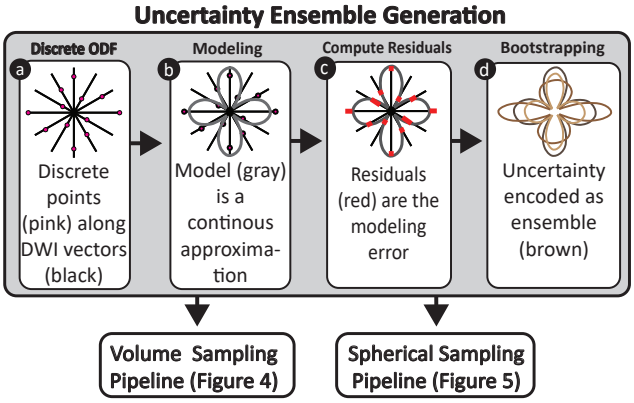

Figure 2: *Overview of the pipeline for encoding model uncertainty as an ODF ensemble. The discrete ODF (a) is measured along each gradient vector, which is then modeled (b) using a continuous basis. The model error is quantified by the residual (c), which is the difference of the discrete ODF and the model's prediction. Bootstrapping creates an ensemble of ODF models (d) based on the residual.*

3.2. Spherical Harmonics

A common HARDI modeling basis, spherical harmonics (SH), is a set of Laplacian eigenfunctions in spherical coordinates [vAPP*11]. An SH basis function is defined as $P(\vec{V}) = Y_l^m(\vec{V})$ where l is the degree and m is the order. Figure 3 shows some shapes of individual basis functions. The SH basis

$$\Psi_{SH}(\vec{V}, B) = \sum_{l=0}^{l_{max}} \sum_{m=-l}^{l} B_l^m Y_l^m(\vec{V}) \tag{2}$$

is a specific implementation of a generic spherical basis (Equation 1) where B is a set of coefficients.

Because of the truncation of the SH basis, it is a low pass approximation. The parameter l_{max} denotes the largest degree l for a truncated SH basis. Because diffusion is symmetric and odd l bands correspond to asymmetry, even l bands are exclusively used. For simplicity, B_l^m and Y_l^m can be redefined with a single coefficient parameter. We define $j_{max} = (l_{max} + 2)(l_{max} + 1)/2$ such that

$$\Psi_{SH}(\vec{V}, B) = \sum_{j=0}^{j_{max}} B_j Y_j(\vec{V}) \tag{3}$$

is a linear redefinition of Equation 2. This redefinition is for convenience as it allows the expression of coefficients B in terms of a single array.

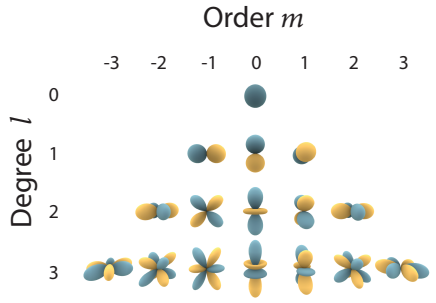

Figure 3: *Table of real spherical harmonics basis up to degree $l = 3$ [Qui14]. The complexity of the basis increases as l increases. Truncation with higher l_{max} can model more prominent ODF directions and separate smaller angles between them. The blue components are positive and the yellow components are negative.*

3.3. Bootstrapping

Analysis and visualization methods only utilizing the initial ODF model Ψ ignore the uncertainty r associated with model fitting. Acquiring redundant scans would be ideal for investigating uncertainty but would be too costly and time-consuming. Therefore, ensemble-based methods resort to statistical analysis to generate sample simulations.

Bootstrapping is a model-agnostic technique to simulate multiple data acquisitions by random residual-based perturbations, as shown in Figure 2d. Two common bootstrapping methods for diffusion imaging are residual bootstrapping and wild bootstrapping [CLH06,Jon08]. Both methods are based on the residual, $r = \hat{S} - S$, which is the difference between the measured signal S and predicted signal $\hat{S}$. The perturbation for residual bootstrapping is determined by random sampling from a pool of all values of r. For wild bootstrapping, the residual is randomly added or subtracted to the measured signal with equal probability. Wild bootstrapping is ideal for SIP functions because it preserves the magnitude of noise variance per vector [JPGJ12].

Wild bootstrapping generates an ODF ensemble for SIP function analysis. Each bootstrap ODF is derived as a set of bootstrap signal coefficients $S^* = [S_1^*, S_2^*, \ldots, S_N^*]$, where $S_n^* \in \hat{S} \pm r$ and $n \in [1, \ldots, N]$. The bootstrap ensemble is defined as a set of corresponding basis function coefficients $A^* = [K(S_1^*), K(S_2^*), \ldots, K(S_N^*)]$. The mapping of S_n^* to a basis function coefficients is $K(S_n^*)$, which is defined in Section 3.1.

3.4. Shape Inclusion Probability

The shape inclusion probability (SIP) function is a powerful statistical tool to analyze shape variation of shape ensembles [LP08]. Jiao et al. investigated the uncertainty of HARDI modeling by analyzing SIP functions of bootstrap ODF ensembles [JPGJ12]. The SIP value at a given point is the fraction of the encompassing shapes, which we also denote as a percentage. If a point p is inside m shapes or bootstrap samples of an ODF ensemble, then the SIP value for the point p is estimated as $\frac{m}{N}$, where N is the number of bootstrap samples. Though the SIP function is model-agnostic, we utilize Ψ_{SH} for the experiments in this paper. Jiao et al. show examples of the SIP function applied to ellpisoid and superquadric tensor glyphs [JPGJ12]. The SIP function

$$\upsilon(p) = 1/N \sum_{n=0}^{N} \begin{cases} 0 & \text{if } |p| > \Psi(\frac{p}{|p|}, A_n) \\ 1 & \text{if } |p| \leq \Psi(\frac{p}{|p|}, A_n) \end{cases} \tag{4}$$

is a discrete value $\upsilon(p) \in [0, 1/N, 2/N, \ldots, 1]$ for an ensemble of N ODF shapes for a point $p \in \mathbb{R}^3$. The distance of the point from the origin, $|p|$, is compared against the distance to the ODF model's surface.

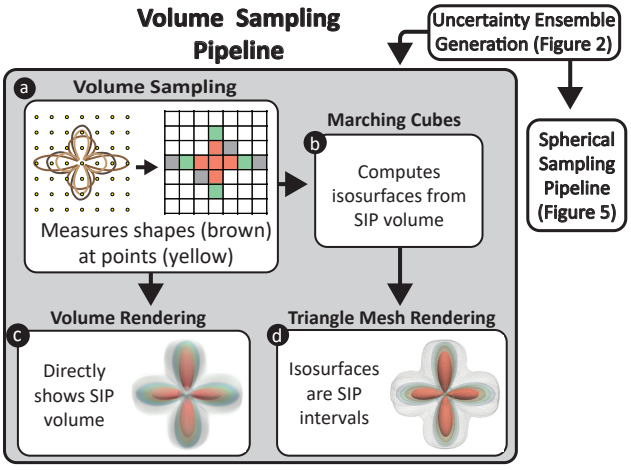

Figure 4: *Overview of the volume sampling [JPGJ12] pipeline for computing and visualizing the SIP function. Volume sampling generates a cubic volume (a) that can be directly volume rendered (c). Isosurfaces can be rendered as triangle meshes (d) by computing marching cubes (b) [LC87].*

Jiao et al. calculate the SIP function at all nodes of a 3D structured volume, which we refer to as the *volume sampling method*, as illustrated in Figure 4a [JPGJ12]. For volume sampling, the SIP value is computed per voxel. Therefore, given a sampling volume of resolution R x R x R, the computational cost of volume sampling is $O(R^3 N)$ per DWI voxel. The high computational and memory cost of volume sampling inhibits integration into HARDI visualization tools. Jiao et al. demonstrate that volume rendering can be directly performed on the SIP function volume [JPGJ12], as shown in Figure 4c and visualized in Figure 1a for a single DWI voxel. However, volume rendering is expensive and requires a lot of memory. An alternative approach is to compute the isosurfaces of the SIP function using marching cubes [LC87], as shown in Figure 4b. These SIP isosurfaces can be rendered as triangle-based meshes, as shown in Figure 4d and visualized in Figure 1b. The isovalues of a SIP isosurface represent the boundaries of its corresponding SIP values. For example, an isosurface with an isovalue of 0.95 would represent the boundary of 95% of the bootstrap shapes. Though this improves rendering performance and storage cost, the slow computation time of the initial volume sampling is still required.

We greatly improve the speed and memory usage for computing the SIP function with our novel approach, *spherical sampling*, as

described in Section 4. By exploiting the properties of HARDI ensembles, the cost of spherical sampling is $O(\Theta^2 N)$ with a sorting complexity of $O(\Theta^2 N \log N)$, where Θ is the polar and azimuthal resolution and N is the number of bootstrap samples. The additional cost of scaling SIP computation to HARDI datasets is discussed in Section 5.

4. Method

4.1. Sampling Sphere

The SIP function can be computed more efficiently with spherical sampling than volume sampling because an ensemble of spherical ODFs maps directly to a spherical basis. Similarly to DWI gradient schemes, the electrostatic repulsion model can determine efficient ODF sampling directions [JHS99]. The simulation of repulsive forces generates a vector set with an evenly spaced distribution. Electrostatic repulsion is an iterative procedure, as there is no perfect solution for all vector sets of size M. Additionally, only a hemisphere needs to be sampled because it is equivalent to a spherical basis due to the symmetric properties of DWI measurements.

Spherical sampling is performed by computing and sorting each surface vertex along a sampling vector for every bootstrap ODF. We define a spherical sampling basis as a set of M ODF sampling directions $\mathbf{C} = [\vec{C}_1, \vec{C}_2, \ldots, \vec{C}_M]$. The surface vertex of an ODF $\Psi(\vec{C}_m, A_n^*)$ is evaluated per sampling direction $\vec{C}_m = [\theta_m, \phi_m]$ for each bootstrap sample A_n^*, where $m \in [1, \ldots, M]$. We discuss the choice of M in Sections 5.3-5.5 and 5.6.

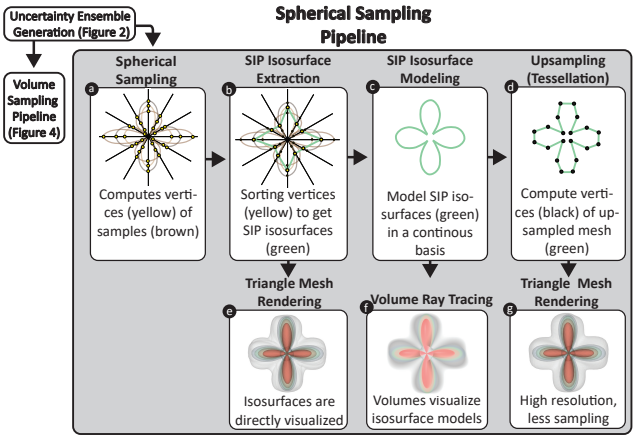

Figure 5: *Overview of the proposed spherical sampling pipeline for computing and visualizing the SIP function. Iso-levels of the SIP function are computed using spherical sampling (a). Extracted isosurfaces (b) can be directly visualized (e). Models of SIP isosurfaces (c) can be visualized with volume ray tracing (f). SIP isosurfaces can also be upsampled (d) and visualized as triangle meshes (g). Only a single SIP isosurface is depicted (b-d).*

4.2. Isosurface Extraction with Spherical Sampling

Spherical sampling enables fast and accurate evaluation of the SIP isosurfaces by exploiting the property that *spherical functions have a unique solution for every spherical coordinate*. Whereas volume

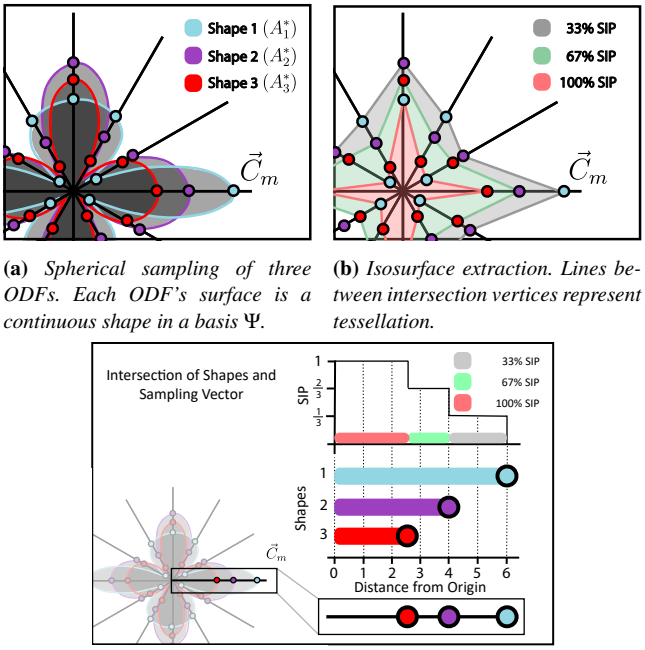

(a) *Spherical sampling of three ODFs. Each ODF's surface is a continuous shape in a basis* Ψ.

(b) *Isosurface extraction. Lines between intersection vertices represent tessellation.*

(c) *Measurement of a SIP function along a sampling vector* ($\vec{C}_m$). *The SIP function is an inverse cumulative distribution function of the shapes' positions.*

Figure 6: *Spherical sampling and isosurface extraction of three ODFs. The ODFs' surface vertices correspond to isolevels of the SIP function, which is shown along a sampling direction* $\vec{C}_m$, *where the dots are the vertices* $\Psi(\vec{C}_m, A_n^*)$ *of the ODF shapes.*

sampling evaluates one SIP value per point, spherical sampling computes all N iso-levels of a SIP function along a sampling vector. Because all ODF shapes reside at a common origin and expand outwards to their boundaries, a SIP function along a sampling direction is guaranteed to be an inverse cumulative distribution function, as shown in Figure 6c. For each sampling direction $\vec{C}_m$, the discrete boundaries of the SIP values are evaluated by computing and sorting the corresponding bootstrap samples' surface offsets, $T_m = [\Psi(\vec{C}_m, A_1^*), \Psi(\vec{C}_m, A_2^*), \ldots, \Psi(\vec{C}_m, A_N^*)]$ (see Eq. 1). Because the SIP function along the sampling direction has probability values in the range $[0,1]$, the sorted array T_m corresponds to the ordered probability boundaries $[1, \ldots, 2/N, 1/N]$. Figure 6a shows an example where an unordered T_m is calculated for $N = 3$ bootstrap samples.

Once all probability boundaries along a sampling direction are computed and sorted, the probability boundaries of interest can then be efficiently extracted, as shown in Figures 5b and 6b. A SIP isosurface of the probability x is defined as a set of surface offsets $H(x) = [T_{1,x}, T_{2,x}, \ldots, T_{M,x}]$. We define U isosurfaces of interest as $I = [H(x_1), H(x_2), \ldots, H(x_U)]$. Each user-defined SIP isosurface $H(x_u)$, where $u \in [1, \ldots, U]$, can be efficiently determined by accessing the sorted array T_m with a corresponding index value

$$d(x, N) = x * N \tag{5}$$

For this definition, index values are assumed to start at one. For

example, the $x = 0.95$ isosurface of the SIP function of $N = 1000$ bootstrap samples will be at index $d = 950$. Additionally, if d is a decimal value, the isosurface can be approximated with interpolation. However, in practice, interpolation can easily be avoided by choosing easily divisible values of x and N.

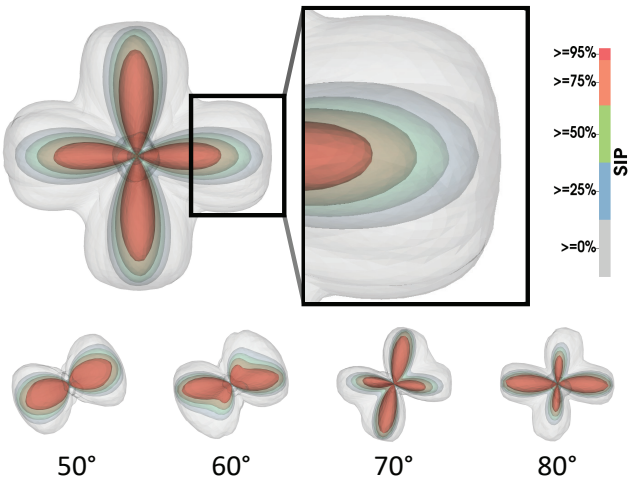

Figure 7: *A set of SIP isosurfaces evaluated with spherical sampling. This method has little error representing a discrete ensemble, which are modeled in a SH basis Ψ_{SH} with $l_{max} = 4$ and M=6,274 samples. More examples with varying angles are shown below.*

Spherical sampling produces accurate SIP isosurfaces because isosurface vertices are computed directly when d is an integer value. Direct SIP isosurface rendering is shown in Figure 5e. Though sampling requirements are high for adequate tessellation, spherical sampling is significantly faster with less data overhead than volume sampling. The faster convergence of this approach is demonstrated in Section 5.3. In Figures 1c and 7, each SIP isosurface is computed and visualized with $M = 6,274$ spherical sampling directions, where modeling was performed with CSD in the SH basis.

4.3. Modeling SIP Isosurfaces

Fitting a model to a SIP isosurface allows efficient upsampling and implicit volume rendering. Modeling is the process of representing a surface as a set of continuous functions. Upsampling SIP isosurfaces allows faster creation of higher resolution polygon meshes. Implicitly volume-rendered glyphs are beneficial because they convey the density of intervals as opacity and do not have the additional error and computational cost from tessellation. We apply the same modeling algorithms for DWI measurements to SIP isosurface vertices, as shown in Figure 5c. Modeling of a SIP isosurface $A'_u = K(H(x_u))$ is represented as coefficients in terms of a basis Ψ' (Equation 1), which provides compact and continuous representation at the cost of some accuracy. The basis for modeling SIP isosurfaces, Ψ', can be independent of the initial modeling basis Ψ. The number of sampling directions, M, is much less for modeling than direct isosurface visualization.

Sampling vectors $\mathbf{C}$ must be carefully chosen to maximize the usefulness of each vector's contribution. We utilize the electrostatic repulsion model to choose sampling vectors that are evenly distributed, which is an established method for choosing DWI vectors [JHS99]. Figure 8 shows the low-resolution SIP isosurfaces $H(x_u)$ used for modeling. Each isosurface in the figure is a discrete mesh with 100 spherical sampling directions, where the initial model was approximated with CSD in a SH basis with $l_{max} = 4$. To minimize error, the SIP function model's complexity, denoted by l'_{max}, should be greater than or equal to the bootstrap ensemble complexity, l_{max}. We discuss this in Section 5.6.

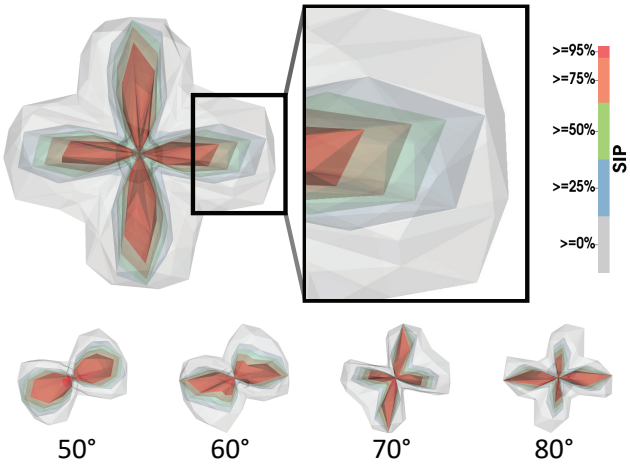

Figure 8: *A set of low-resolution SIP isosurfaces evaluated with spherical sampling for upsampling and ray tracing. The ensemble is modeled in a SH basis Ψ_{SH} with $l_{max} = 4$ and $M = 100$ sampling directions. More examples with varying angles are shown below.*

4.4. Upsampling SIP Isosurfaces

Upsampling a SIP isosurface from a model Ψ' is much cheaper than extraction from spherical sampling(Section 4.2). Upsampling is the process of converting a low-resolution dataset to a high-resolution one by interpolation. The preliminary step of low-resolution sampling and modeling of SIP isosurfaces is described in Section 4.3. Tessellation of SIP isosurface models is illustrated in Figure 5d, which is directly rendered as triangle-based meshes in Figure 5g. A higher resolution mesh representation can be computed from evaluating the SIP isosurface models with a modeling basis $\Psi'(\vec{C}'_m, A'_u)$ at spherical sampling directions $\mathbf{C}' = [\vec{C}'_1, \vec{C}'_1, \ldots, \vec{C}'_{M'}]$, where $M' > M$. The number of ODF model evaluations for the SIP computation is $N * M$, where N is the number of bootstrap samples and M is the number of sampling directions. In contrast, the number of model evaluations for computing SIP isosurfaces is $U * M'$. Typically, the number of SIP isosurfaces of interest, U is significantly lower than N, resulting in much faster tessellation.

Upsampling creates a smoother, more aesthetically pleasing image at a lower computational cost. Because this approach is a form of approximation, there will be some error depending on the choice of parameters, as presented in our results in Section 5.6. In Figure 9, the SIP function is evaluated with $M = 100$ sampling directions, all five SIP isosurfaces are modeled, and then the new isosurfaces

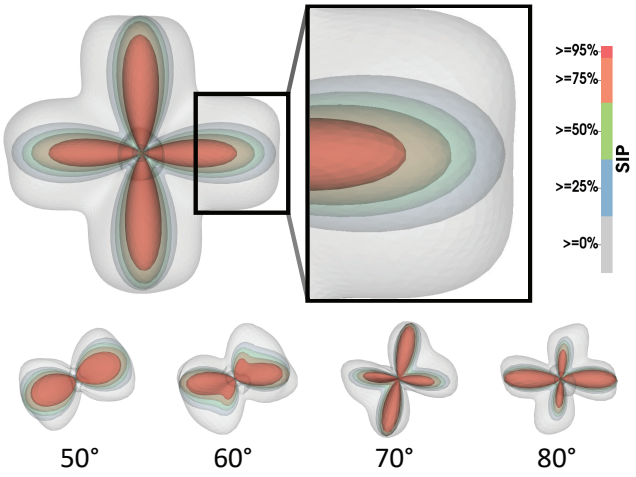

Figure 9: *Upsampling SIP isosurfaces from SH models. Models of SIP isosurfaces can be efficiently tessellated and provide smoother representation. The ODF ensemble is modeled in a SH basis Ψ_{SH} of $l_{max} = 4$ with $M = 100$ sampling directions. SIP isosurfaces are modeled in a SH basis Ψ'_{SH} of $l'_{max} = 8$ with $M' = 6,274$ sampling directions. More examples with varying angles are shown below.*

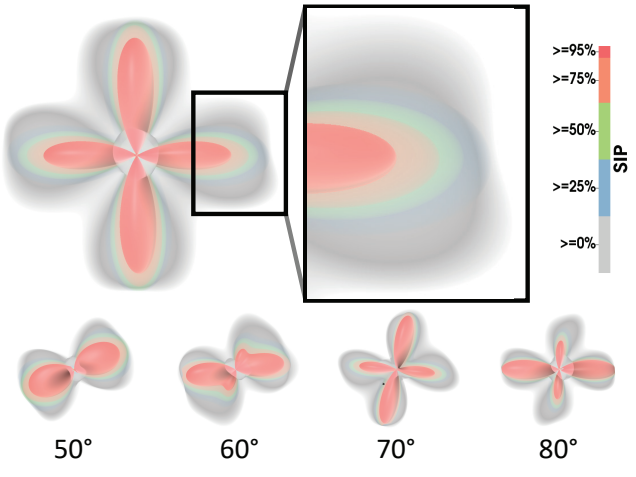

Figure 10: *Implicit ray tracing of a volumetric SIP glyph allows for fast sampling and provides smooth representation without needing tessellation. The SIP isosurfaces are modeled in a SH Basis Ψ_{SH} of $l'_{max} = 8$ with $M = 100$ sampling directions. The volume extinction values are σ(Outer to Inner)$= [1.8, 2.5, 3.5]$ with an opaque innermost surface. More examples with varying angles are shown below.*

are tessellated from the SIP isosurface models with $M' = 6,274$ sampling directions. The number of sampling directions used to compute the SIP function is equivalent to Figure 8, while the isosurface resolution is equivalent to Figure 7.

4.5. Implicitly Rendered SIP Glyph using SH Ray Tracing

Additionally, modeling SIP isosurfaces with a continuous basis Ψ' enables implicit ray tracing. For SIP glyph visualization, implicit rendering reduces data overhead by eliminating the need for tessellation while rendering a continuously smooth shape, as shown in Figure 5f. Rendering of transparent surfaces and volumes requires multiple intersections to be computed per isosurface, which is simultaneously computed by ray tracing of implicit shapes in the SH basis Ψ_{SH} [PPUJ23]. Peters et al. introduced a fast implicit SH ray tracing method and an extension for uncertainty visualization by rendering uncertain regions as transparent surfaces or volumes. However, Peter et al.'s uncertainty visualization method lacks a pipeline for computing the necessary uncertainty data. Modeling of SIP isosurfaces, as described in Section 4.3, provides the missing computation method for their implicit uncertainty glyphs.

We apply Peter et al.'s uncertainty glyph rendering technique to SIP functions. In comparison, we visualize the SIP function with multiple transparent volumes. To prevent smaller, more certain volumes from being occluded, we assign lower opacity values to the larger, less certain volumes. The volumetric transmittance is defined as $\exp(-\sigma d)$ where $\sigma > 0$ is a user-defined extinction parameter, and $d \geq 0$ is the distance the ray has traveled through the volume. To adjust each volumetric region's opacity individually, we assign different σ values per volume. Figures 1d and 10 show an example of this uncertainty glyph with four volumetric regions where σ increases with each subsequent region. The implicit rendering of the uncertainty glyphs was performed with Intel OSPRay [WJA*17] using a custom geometry module and renderer.

5. Results and Discussion

5.1. Synthetic Data

To evaluate the SIP isosurface accuracy, we construct synthetic data using the tensor multi-compartment model [TRW*02]. This synthetic dataset is used in Figures 1, 7-10, and 12. Since the primary goal of HARDI research is to distinguish multiple fibers, we simulate data with two crossing fibers with varying angles. For both tensors, we simulate eigenvalues $[\lambda_1, \lambda_2, \lambda_3] = [1900, 100, 100] * 10^{-6}$ mm^2/s [Des08]. We use a b-value of 2000 s/mm^2 with an signal-to-noise ratio (SNR) of ten. The b-values denote the gradient strength and duration of an MR field. Because the choice of SNR and b-value affects the SIP function, we chose a common b-value for HARDI. We chose a high noise value, SNR of five, to make confidence intervals larger for inspection. Jiao et al. further detail how a variation of b-values and SNR values affect SIP functions [JPGJ12]. For modeling, we used a response function with the same eigenvalues as the input tensors. While the response function is typically computed from the most linear voxels of a dataset, the response function of our synthetic example is known.

5.2. Human-Brain Data

The main benefit of the spherical sampling approach is that the efficiency of evaluating SIP functions υ is viable for application to larger datasets. We show this by applying it to Stanford's human-brain HARDI dataset [RYP*15], which has a DWI volume resolution of 81x106x76. The scanner was a 3T GE Discovery MRI system. The data used from the study measured 10 non-diffusion weighted images (b0) and 150 images diffusion weighted with a

b-value of 2000 s/mm^2. The b-value is a measure of the degree of diffusion-weighting. Non-diffusion weighted images (b0) are acquired as a baseline for diffusion measurements. Figure 11 shows an entire transverse slice of the Stanford dataset visualized with SIP isosurface glyphs. The initial modeling $K(S) = A$ in the SH basis Ψ_{SH} with $l_{max} = 4$ is performed with the diffusion analysis library, Dipy [GBA*14]. The SIP functions υ are evaluated with $N = 1000$ bootstrap samples (Section 3.3) and $M = 100$ sampling vectors (Section 4.1) to extract $U = 5$ isosurface of interest, where each individual isosurface is defined as $H(x_u)$. We then model each SIP isosurface (Sections 4.2-4.3) by mapping to the SH basis as $A'_u = K(H(x_u))$. The model is subsequently tessellated with $M' = 500$ vectors (Section 4.4).

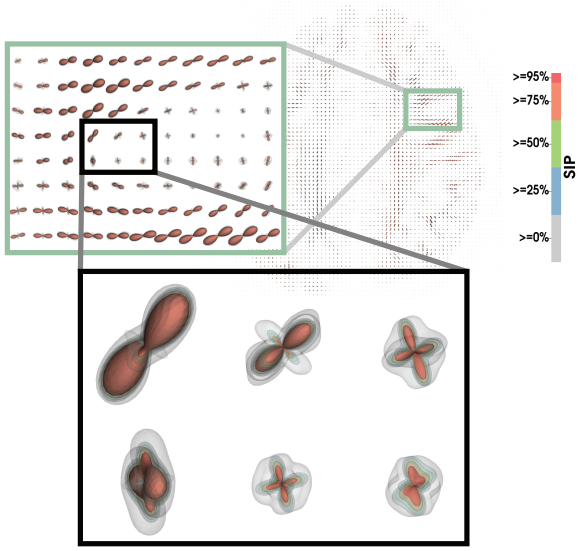

Figure 11: *A slice of the Stanford HARDI dataset with glyphs of SIP isosurfaces intuitively shows ODF model uncertainty. The ensemble is modeled in a SH basis Ψ_{SH} of $l_{max} = 4$ and sampled with $M = 100$ directions. The SIP isosurfaces were modeled in a SH basis Ψ'_{SH} of $l'_{max} = 8$ and tessellated with $M' = 1000$ directions.*

5.3. Accuracy

Spherical sampling converges faster than volume sampling. We define the SIP isosurface error as $x - \upsilon(p)$, which is the difference between the representative iso-level x and the expected SIP value $\upsilon(p)$ (Equation 4) at point p on the SIP isosurface. We measure the errors at isosurface vertices and sampled points on the isosurfaces. Because spherical sampling directly computes probability boundaries, the SIP isosurface error at the vertices is very low. Consequently, SIP isosurface error quickly converges to zero as the isosurface resolution increases, as shown in Figure 12. The error is computed from 35 seeds. Though more seeds would have been ideal, the computation time of volume sampling constrained how many were feasible to analyze. However, each measurement is evaluated from 1000 measurements for each of the 10 different iso-levels per seed. Additionally, computing a predicted iso-level x from a SIP volume requires first extracting SIP isosurfaces with an isosurface technique such as marching cubes [LC87]. Because implicitly rendered glyphs (Section 4.5) don't apply tessellation, the SIP isosurface error is only introduced from modeling, which is described in Section 5.6. Upsampled glyphs (Section 4.4) introduce errors from both tessellation and modeling.

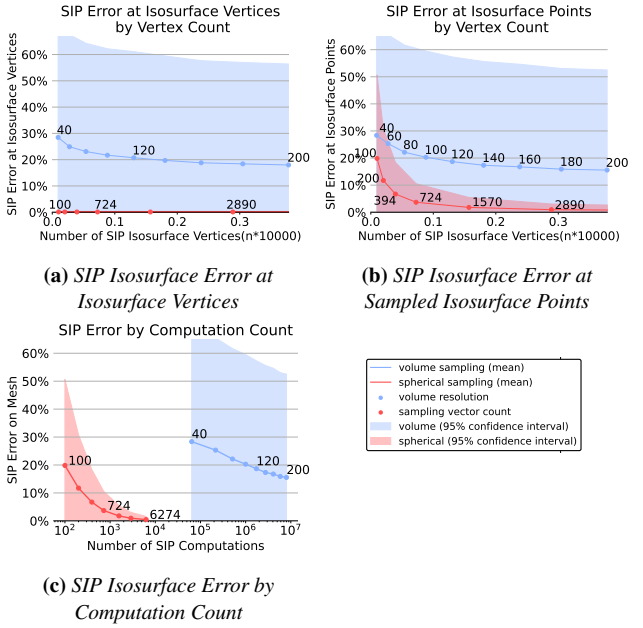

(a) *SIP Isosurface Error at Isosurface Vertices*

(b) *SIP Isosurface Error at Sampled Isosurface Points*

(c) *SIP Isosurface Error by Computation Count*

Figure 12: *The SIP error for our spherical sampling method (red) converges faster than volume sampling (blue) with regards to resolutions (a & b) and number of computations (c). The shaded region represents a 95% confidence interval. The results are an average of iso-levels ranging from 0 to 1 with increments of 0.05. The test data is described in Section 5.1. Results were computed from 35 randomization seeds for computing bootstrap samples.*

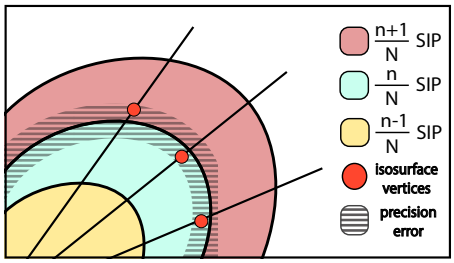

Figure 13: *Illustration of the magnitude of SIP isosurface error with spherical sampling. For a SIP isosurface of isovalue $\frac{n}{N}$, the SIP isosurface error is on the scale of precision error. In our experiments, the error is less than $1e^{-12}$. The SIP value of a point evaluates to $\frac{n}{N}$ (blue) or $\frac{n+1}{N}$ (red) depending on the precision error. The SIP isosurface vertices are red. The shaded area marks the precision error.*

Spherical sampling exhibits minimal SIP isosurface error at vertices because those vertices lie on the corresponding probability boundary, as illustrated in Figure 13. Because the iso-level calculation is inaccurate by an order of machine precision, the measured

SIP isosurface error will be either zero or $1/N$. Volume sampling evaluates SIP values at the center of voxels, which are not likely to correspond to iso-levels. Figure 12a shows this relationship by measuring the SIP isosurface error of both methods at isosurface vertices. The error from modeling is discussed in Section 5.6.

Measuring SIP isosurface error at sampled isosurface points also demonstrates better accuracy with spherical sampling. Though the SIP isosurface error at the vertices is near zero for spherical sampling, the error of a point sampled on the isosurface depends on the resolution because tessellation is a form of linear interpolation between vertices. As resolution increases, the SIP isosurface error converges to zero. The average error of the isosurface is measured by Monte Carlo integration of random points that lie on the isosurface. Though both volume and spherical sampling converge as their resolution increases, spherical sampling converges more rapidly. Figure 12b shows the change in error as resolution increases with regards to isosurface resolution. Figure 12c shows the difference in the convergence rate regarding the number of SIP computations.

Though spherical sampling reduces the SIP isosurface error, it is independent the SIP error introduced by Jiao et al. [JPGJ12]. The SIP error is determined by the basis complexity and number of bootstrap samples. Jiao et al. define the maximum SIP error as $\sqrt{(1/2N)(\nu + ln(1/\delta))}$ with probability $1-\delta$ for N bootstrap samples where ν is the number of SH basis coefficients. In Figure 12, the data is generated with $N = 1000$ bootstrap samples and $\nu = 15$, which results in 99% of all SIP function samples having at most 10% error. Jiao et al. state that this error will be much less for most samples [JPGJ12]. In contrast to the SIP isosurface error measured in Figure 12b, volume sampling of resolution 200 can have a mean error of 8.1% and the 95% confidence interval can be up to 30.8%. In comparison, spherical sampling with 1570 and 6274 sampling vectors resulted in a mean error of 1.1% and 0.3% and a 95% confidence interval of 3.1% and 0.8% respectively. In our experiments, the error from spherical sampling was less than the SIP error resulting from limited bootstrap samples, unlike volume sampling.

5.4. Speed

Spherical sampling exhibits a much faster computation time than the state-of-the-art volume sampling approach. Volume sampling exhibits quartic $O(R^3N)$ complexity, where R is the resolution of sampling volume and N is the number of bootstrap samples. In volume sampling, each voxel of the sampling volume must evaluate the distance from the origin to the isosurface vertices of all N bootstrap samples. The key insight to improving performance is that evaluating N bootstrap samples provides N iso-levels along all directions. Whereas volume sampling only records the percentage of encompassing shapes at a single point, spherical sampling records all N iso-levels along a vector. For spherical sampling, the volume resolution R x R x R is replaced with the polar and azimuthal resolution of the sampling sphere, Θ x Θ, which would result in a complexity of $O(\Theta^2 N)$. In our experiments, we sort arrays with the Timsort algorithm [Pet02] which has a time complexity of $O(\Theta^2 N \log N)$. For a set of M sampling vectors, the angular resolution Θ can be approximated as $\Theta \approx \sqrt{M}$.

Table 1 shows the compute time of the volume and spherical sampling methods, with and without upsampling. Direct SIP isosurface extraction with $M = 1000$ is 3228× faster than volume sampling with $R = 200$. Upsampling SIP isosurfaces with the SH basis Ψ'_{SH} provides additional performance. The upsampled SIP isosurfaces of similar resolution with $l'_{max} = 8$, $M = 100$, and $M' = 1000$ are 8164× faster than volume sampling with $R = 200$. All the measurements are performed on an Intel i9-12900K CPU with 128GB RAM with a multi-threaded Python script using the diffusion analysis library, Dipy [GBA*14]. Only generating bootstrap samples and evaluating the SIP function is measured because the cost of generating bootstrap samples is consistent between all methods.

$l_{max} = 4, N = 1000$	Compute Time per Voxel	Compute Time per Slice (81,106)
Volume Sampling($R = 100$)	2 min 1 sec	12.02 days (estimate)
Volume Sampling($R = 200$)	11 min 34 sec	68.97 days(estimate)
Direct SIP Isosurface ($M = 500$)	114 ms	12 min 10 sec
Direct SIP Isosurface ($M = 1000$)	215 ms	24 min 20 sec
Upsampled SIP Isosurface ($l'_{max} = 4$, $M = 60, M' = 1000$)	31 ms	4 min 30 sec
Upsampled SIP Isosurface ($l'_{max} = 8$, $M = 100, M' = 1000$)	85 ms	13 min 17 sec

Table 1: *Superior computational performance of our spherical sampling method over volume sampling. Spherical sampling is used for direct computed SIP isosurfaces (Section 4.2) shown in orange and the upsampling method (Section 4.4) shown in pink. The dataset used is a slice of the Stanford HARDI brain data (Section 5.2).*

The spherical sampling method drastically reduces the computation time over volume sampling in our experiments. Our upsampling method provides an additional performance improvement. The main benefit is making it feasible to compute whole slices of real data. This increase in speed could make SIP function computation more viable in clinical applications where time is limited.

5.5. Memory

The memory constraints of volume sampling previously limited the applicability of analyzing SIP functions of real HARDI datasets. Table 2 shows the volume and spherical sampling's memory requirements. Compared to a volume of $R = 200$, a polygon mesh of $M = 1000$ reduces the storage size by 1638× and a SH model of $l'_{max} = 8$ reduces the storage size by 37282×. With spherical sampling, the memory scales by the number of isosurfaces P, whereas the volume sampling method stores an entire volume of isovalues per DWI voxel. The full memory profile of volume sampling is unnecessary because visualizing over eight confidence intervals is not useful [JPGJ12]. Although SIP isosurfaces can be extracted from the volume sampling approach by marching cubes [LC87], accu-

racy and speed are still worse than the spherical sampling method. We discuss these differences further in Sections 5.3 and 5.4.

SIP Interval Modeling	Single Voxel	Slice of Stanford Data (81,106)
Volume(100^3)	4MB	33.54 GB
Volume(200^3)	32MB	268.31 GB
Polygon Mesh(M=500)	10 KB	83.8 MB
Polygon Mesh(M=1,000)	20 KB	167.7 MB
Polygon Mesh(M=10,000)	200 KB	1.68 GB
SH Basis $l'_{max} = 4$	300 B	2.58 MB
SH Basis $l'_{max} = 8$	900 B	7.75 MB
SH Basis $l'_{max} = 12$	1.82 KB	15.65 MB

Table 2: *The memory overhead is greatly reduced with spherical sampling methods. Modeling of SIP isosurfaces with spherical harmonics (SH) provides additional storage reduction. Five isosurfaces are computed for polygon meshes and SH models. Gray is volume sampling (Section 3.4) and orange is the tessellated SIP isosurfaces of spherical sampling (Sections 4.2 and 4.4), and the purple is SH modeling of SIP isosurfaces (Sections 4.3 and 4.5). The data sets are described in Sections 5.1 and 5.2. l'_{max} is the degree of complexity of the SH basis Ψ_{SH}.*

The representation of SIP functions as cubic volumes has a high storage cost, making it difficult to store in the limited RAM of desktop computers. We showed that this limitation can be overcome by representing SIP isosurfaces as polygon meshes. An additional storage reduction is achieved by modeling with the SH basis.

5.6. Relationship of SH Degree and Sampling Sphere Resolution

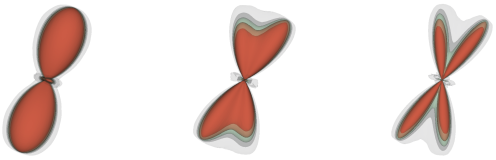

(a) $l_{max} = 4$ **(b)** $l_{max} = 8$ **(c)** $l_{max} = 12$

Figure 14: *Higher maximum SH degree (l_{max}) values can discern smaller fiber angles. The ensemble is modeled with varying l_{max} degrees to show the consequent angle separations. SIP functions of higher ensemble l_{max} are computed with more bootstrap samples.*

Computing SIP functions of ODF ensembles of higher SH degree results in better fiber angle separation. Figure 14 shows the improved angle separation when the SH degree l_{max} increases. More bootstrap samples are simulated to use higher SH degrees [JPGJ12], so $N = 5000$ bootstrap samples are used in Figure 14.

Increasing the SH degree of the bootstrap models requires increasing the SH degree of the SIP isosurface models and the number of sampling vectors. This relationship is shown in Figure 15, where the SIP isosurface error decreases as the number of sampling

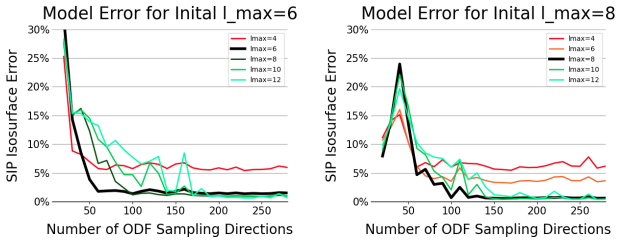

(a) *Model* $l_{max} = 6$ **(b)** *Model* $l_{max} = 8$

Figure 15: *The SIP isosurface error decreases as the number of ODF sampling vectors increases. The error of SIP isosurface modeling achieves lower minimum error when the SIP isosurface model's complexity l'_{max} is greater than or equal to the bootstrap samples' complexity l_{max}. However, higher l'_{max} requires more sampling directions to converge. Black lines are where $l'_{max} = l_{max}$, red lines are where $l'_{max} < l_{max}$, and green lines are where $l'_{max} > l_{max}$.*

vectors increases. The SIP isosurface error is measured at isosurface vertices to exclude the error introduced from tessellation. The error is significant when the SIP isosurface model's SH degree l'_{max} is less than the bootstrap samples' SH degree l_{max} because the SIP isosurface model has fewer degrees of freedom than the models it represents. As shown in Figure 15a, a SIP isosurface represented with a SH basis of $l'_{max} = 4$ for initial models represented with $l_{max} = 6$ maintains higher SIP isosurface error. Similarly, in Figure 15b, the SIP isosurface error is higher when modeled with a SH basis of $l'_{max} = 4$ and $l'_{max} = 6$ for initial models represented with $l_{max} = 8$. Therefore, SIP isosurface models should have equal or greater degrees of freedom than the model for ODF ensembles.

6. Conclusion and Future Work

Our novel spherical sampling method addresses the performance limitations of the volume sampling method [JPGJ12] by computing SIP functions in a fast, accurate, and memory-efficient manner. In our experiments, SIP isosurfaces extracted and upsampled with our spherical sampling approach achieved up to 8164× speedup, 37282× memory reduction, and 50.2% less SIP isosurface error compared to the volume sampling method.

Though we primarily showcase SIP isosurface modeling for uncertainty glyph visualization, SIP functions may find utility in informing decisions of choosing paths for uncertainty-based tractography. The isosurfaces of the SIP function could also be used to derive novel statistical scalar invariants. Extending interpolation techniques to SIP functions is yet to be explored, which is integral to tractography and glyph placement strategies. Uncertainty analysis of the SIP function could be useful in studying the impact of scanner acquisition techniques. In addition, GPU hardware could be utilized to improve performance for quickly processing entire data sets or increasing resolution. Fast SIP function analysis enables many new avenues of HARDI uncertainty exploration.

7. Acknoledgements

This work was supported in part by the Intel Center of Excellence and the U.S. Department of En- ergy (DOE) RAPIDS-2 SciDAC project under contract number DE- AC0500OR22725.

References

[ALS*10] AGANJ I., LENGLET C., SAPIRO G., YACOUB E., UGURBIL K., HAREL N.: Reconstruction of the orientation distribution function in single- and multiple-shell q-ball imaging within constant solid angle. *Magnetic Resonance in Medicine 64*, 2 (2010), 554–566. URL: https://onlinelibrary.wiley.com/doi/abs/10.1002/mrm.22365, arXiv:https://onlinelibrary.wiley.com/doi/pdf/10.1002/mrm.22365, doi:https://doi.org/10.1002/mrm.22365. 3

[AWHS16] ABBASLOO A., WIENS V., HERMANN M., SCHULTZ T.: Visualizing tensor normal distributions at multiple levels of detail. *IEEE Transactions on Visualization and Computer Graphics 22*, 1 (Jan. 2016), 975–984. URL: https://doi.org/10.1109/TVCG.2015.2467031, doi:10.1109/TVCG.2015.2467031. 3

[BHK*14] BAUER C. M., HEIDARY G., KOO B.-B., KILLIANY R. J., BEX P., MERABET L. B.: Abnormal white matter tractography of visual pathways detected by high-angular-resolution diffusion imaging (HARDI) corresponds to visual dysfunction in cortical/cerebral visual impairment. *Journal of American Association for Pediatric Ophthalmology and Strabismus 18*, 4 (Aug. 2014), 398–401. doi:10.1016/j.jaapos.2014.03.004. 2

[BHZ*17] BAUER C. M., HIRSCH G. V., ZAJAC L., KOO B.-B., COLLIGNON O., MERABET L. B.: Multimodal MR-imaging reveals large-scale structural and functional connectivity changes in profound early blindness. *PLOS ONE 12*, 3 (Mar. 2017), e0173064. doi:10.1371/journal.pone.0173064. 2

[BML94] BASSER P. J., MATTIELLO J., LEBIHAN D.: MR diffusion tensor spectroscopy and imaging. *Biophysical Journal 66*, 1 (Jan. 1994), 259–267. doi:10.1016/S0006-3495(94)80775-1. 2

[BOL12] BRODLIE K., OSORIO R. A., LOPES A.: A review of uncertainty in data visualization. In *Expanding the Frontiers of Visual Analytics and Visualization*, Dill J., Earnshaw R., Kasik D., Vince J., Wong P. C., (Eds.). Springer Verlag London, 2012, pp. 81–109. 2

[BPP*00] BASSER P. J., PAJEVIC S., PIERPAOLI C., DUDA J., ALDROUBI A.: In vivo fiber tractography using DT-MRI data. *Magnetic Resonance in Medicine 44*, 4 (2000), 625–632. doi:10.1002/1522-2594(200010)44:4<625::AID-MRM17>3.0.CO;2-O. 2

[BPtHRV13] BRECHEISEN R., PLATEL B., TER HAAR ROMENY B. M., VILANOVA A.: Illustrative uncertainty visualization of DTI fiber pathways. *The Visual Computer 29*, 4 (Apr. 2013), 297–309. URL: https://doi.org/10.1007/s00371-012-0733-9, doi:10.1007/s00371-012-0733-9. 2

[BVF08] BARMPOUTIS A., VEMURI B. C., FORDER J. R.: Fast displacement probability profile approximation from HARDI using 4th-order tensors. In *2008 5th IEEE International Symposium on Biomedical Imaging: From Nano to Macro* (May 2008), pp. 911–914. doi:10.1109/ISBI.2008.4541145. 2

[CADW11] COHEN-ADAD J., DESCOTEAUX M., WALD L. L.: Quality assessment of high angular resolution diffusion imaging data using bootstrap on q-ball reconstruction. *Journal of Magnetic Resonance Imaging 33*, 5 (2011), 1194–1208. doi:https://doi.org/10.1002/jmri.22535. 3

[Cal19] CALAMANTE F.: The seven deadly sins of measuring brain structural connectivity using diffusion mri streamlines fibre-tracking. *Diagnostics 9* (2019). URL: https://api.semanticscholar.org/CorpusID:202402773. 2

[CLH06] CHUNG S., LU Y., HENRY R. G.: Comparison of bootstrap approaches for estimation of uncertainties of DTI parameters. *NeuroImage 33*, 2 (Nov. 2006), 531–541. doi:10.1016/j.neuroimage.2006.07.001. 2, 4

[CZCE08] CHEN W., ZHANG S., CORREIA S., EBERT D. S.: Abstractive Representation and Exploration of Hierarchically Clustered Diffusion Tensor Fiber Tracts. *Computer Graphics Forum 27*, 3 (2008), 1071–1078. doi:10.1111/j.1467-8659.2008.01244.x. 2

[Des08] DESCOTEAUX M.: *High Angular Resolution Diffusion MRI: from Local Estimation to Segmentation and Tractography*. phdthesis, Université Nice Sophia Antipolis, Feb. 2008. URL: https://theses.hal.science/tel-00457458. 7

[ESM*05] ENDERS F., SAUBER N., MERHOF D., HASTREITER P., NIMSKY C., STAMMINGER M.: Visualization of white matter tracts with wrapped streamlines. In *VIS 05. IEEE Visualization, 2005.* (Oct. 2005), pp. 51–58. doi:10.1109/VISUAL.2005.1532777. 2

[Fra02] FRANK L. R.: Characterization of anisotropy in high angular resolution diffusion-weighted mri. *Magnetic Resonance in Medicine 47*, 6 (2002), 1083–1099. doi:https://doi.org/10.1002/mrm.10156. 2

[GBA*14] GARYFALLIDIS E., BRETT M., AMIRBEKIAN B., ROKEM A., VAN DER WALT S., DESCOTEAUX M., NIMMO-SMITH I.: Dipy, a library for the analysis of diffusion MRI data. *Frontiers in Neuroinformatics 8* (2014). 8, 9

[GRT19] GERRITS T., ROESSL C., THEISEL H.: Towards glyphs for uncertain symmetric Second-Order tensors. *Computer Graphics Forum 38* (June 2019), 325–336. doi:10.1111/cgf.13692. 3

[HRC*11] HAROON H., REYNOLDS H., CARTER S., EMBLETON K., HERHOLZ K., PARKER G.: HARDI-based microstructural complexity mapping reveals distinct subcortical and cortical grey matter changes in mild cognitive impairment and Alzheimer's disease. *Proc Int Soc Mag Reson Med* (Jan. 2011). 2, 3

[JHS99] JONES D., HORSFIELD M., SIMMONS A.: Optimal strategies for measuring diffusion in anisotropic systems by magnetic resonance imaging. *Magnetic Resonance in Medicine 42*, 3 (1999), 515–525. doi:10.1002/(SICI)1522-2594(199909)42:3<515::AID-MRM14>3.0.CO;2-Q. 5, 6

[JJ11] JBABDI S., JOHANSEN-BERG H.: Tractography: Where Do We Go from Here? *Brain Connectivity 1*, 3 (Sept. 2011), 169–183. doi:10.1089/brain.2011.0033. 2

[Joh04] JOHNSON C. R.: Top scientific visualization research problems. *IEEE Computer Graphics and Applications 24*, 4 (2004), 13–17. doi:10.1109/MCG.2004.20. 2

[Jon03] JONES D. K.: Determining and visualizing uncertainty in estimates of fiber orientation from diffusion tensor MRI. *Magnetic Resonance in Medicine 49* (2003), 7–12. 3

[Jon08] JONES D. K.: Tractography gone wild: Probabilistic fibre tracking using the wild bootstrap with diffusion tensor MRI. *IEEE transactions on medical imaging 27*, 9 (Sept. 2008), 1268–1274. doi:10.1109/TMI.2008.922191. 2, 4

[JPGJ12] JIAO F., PHILLIPS J., GUR Y., JOHNSON C. R.: Uncertainty visualization in HARDI based on ensembles of ODFs. *IEEE Pacific Visualization Symposium : [proceedings]. IEEE Pacific Visualisation Symposium 2013* (Dec. 2012), 193–200. doi:10.1109/PacificVis.2012.6183591. 1, 2, 3, 4, 7, 9, 10

[JS03] JOHNSON C. R., SANDERSON A. R.: A next step: Visualizing errors and uncertainty. *IEEE Computer Graphics and Applications 23*, 5 (Sept.-Oct. 2003), 6–10. doi:10.1109/MCG.2003.1231171. 2

[Kin04] KINDLMANN G.: Superquadric tensor glyphs. *Visualization (VisSym), EG/IEEE TCVG Symposium on* (Jan. 2004), 147–154. doi:10.2312/VisSym/VisSym04/147-154. 2

[LC87] LORENSEN W. E., CLINE H. E.: Marching cubes: A high resolution 3D surface construction algorithm. *SIGGRAPH Comput. Graph. 21*, 4 (Aug. 1987), 163–169. Number of pages: 7 Place: New York, NY, USA Publisher: Association for Computing Machinery tex.issue_date: July 1987. URL: https://doi.org/10.1145/37402.37422, doi:10.1145/37402.37422. 4, 8, 9

[LP08] LOFFLER M., PHILLIPS J. M.: Shape Fitting on Point Sets with Probability Distributions, Dec. 2008. arXiv:0812.2967 [cs]. URL: http://arxiv.org/abs/0812.2967, doi:10.48550/arXiv.0812.2967. 3, 4

[MD13] MERLET S. L., DERICHE R.: Continuous diffusion signal, EAP and ODF estimation via Compressive Sensing in diffusion MRI. *Medical Image Analysis 17*, 5 (July 2013), 556–572. doi:10.1016/j.media.2013.02.010. 2

[MMB*09] MERHOF D., MEISTER M., BINGOL E., NIMSKY C., GREINER G.: Isosurface-based generation of hulls encompassing neuronal pathways. *Stereotactic and Functional Neurosurgery 87*, 1 (2009), 50–60. doi:10.1159/000195720. 2

[MR10] MICHAILOVICH O., RATHI Y.: Fast and Accurate Reconstruction of HARDI Data Using Compressed Sensing. In *Medical Image Computing and Computer-Assisted Intervention – MICCAI 2010* (Berlin, Heidelberg, 2010), Jiang T., Navab N., Pluim J. P. W., Viergever M. A., (Eds.), Lecture Notes in Computer Science, Springer, pp. 607–614. doi:10.1007/978-3-642-15705-9_74. 2

[MRS10] MICHAILOVICH O., RATHI Y., SHENTON M. E.: On Approximation of Orientation Distributions by means of Spherical Ridgelets. *IEEE transactions on image processing : a publication of the IEEE Signal Processing Society 19*, 2 (Feb. 2010), 461–477. doi:10.1109/TIP.2009.2035886. 2

[MVYM06] MCGRAW T., VEMURI B. C., YEZIERSKI B., MARECI T.: VON MISES-FISHER MIXTURE MODEL OF THE DIFFUSION ODF. *Proceedings / IEEE International Symposium on Biomedical Imaging: from nano to macro. IEEE International Symposium on Biomedical Imaging 2006* (2006), 65–68. doi:10.1109/ISBI.2006.1624853. 2

[ODWL19] O'DONNELL L. J., DADUCCI A., WASSERMANN D., LENGLET C.: Advances in computational and statistical diffusion MRI. *NMR in Biomedicine 32*, 4 (2019), e3805. doi:10.1002/nbm.3805. 2

[OVVDW10] OTTEN R., VILANOVA A., VAN DE WETERING H.: Illustrative White Matter Fiber Bundles. *Computer Graphics Forum 29*, 3 (2010), 1013–1022. doi:10.1111/j.1467-8659.2009.01688.x. 2

[Pet02] PETERS T.:, 2002. URL: https://bugs.python.org/file4451/timsort.txt?ref=skerritt.blog. 9

[PPUJ23] PETERS C., PATEL T., USHER W., JOHNSON C. R.: Ray Tracing Spherical Harmonics Glyphs. In *Vision, Modeling, and Visualization* (2023), Guthe M., Grosch T., (Eds.), The Eurographics Association, pp. 21–31. doi:10.2312/vmv.20231223. 2, 3, 7

[PPvA*09] PEETERS T., PRCKOVSKA V., VAN ALMSICK M., VILANOVA A., TER HAAR ROMENY B.: Fast and sleek glyph rendering for interactive HARDI data exploration. In *2009 IEEE pacific visualization symposium* (2009), pp. 153–160. 2

[PWP*15] PUJOL S., WELLS W., PIERPAOLI C., BRUN C., GEE J., CHENG G., VEMURI B., COMMOWICK O., PRIMA S., STAMM A., GOUBRAN M., KHAN A., PETERS T., NEHER P., MAIER-HEIN K. H., SHI Y., TRISTAN-VEGA A., VENI G., WHITAKER R., STYNER M., WESTIN C.-F., GOUTTARD S., NORTON I., CHAUVIN L., MAMATA H., GERIG G., NABAVI A., GOLBY A., KIKINIS R.: The DTI Challenge: Toward Standardized Evaluation of Diffusion Tensor Imaging Tractography for Neurosurgery. *Journal of Neuroimaging 25*, 6 (2015), 875–882. doi:10.1111/jon.12283. 3

[Qui14] QUILEZ I.: Spherical harmonics, 2014. Image used under the Creative Commons Attribution-ShareAlike license. URL: https://commons.wikimedia.org/wiki/File:Spherical_Harmonics.png. 4

[RYP*15] ROKEM A., YEATMAN J. D., PESTILLI F., KAY K. N., MEZER A., VAN DER WALT S., WANDELL B. A.: Correction: Evaluating the accuracy of diffusion mri models in white matter. *PLOS ONE 10*, 9 (09 2015), 1–1. URL: https://doi.org/10.1371/journal.pone.0139150, doi:10.1371/journal.pone.0139150. 7

[SG24] SCHMITZ T., GERRITS T.: Exploring uncertainty visualization for degenerate tensors in 3d symmetric second-order tensor field ensembles. In *2024 IEEE Workshop on Uncertainty Visualization: Applications, Techniques, Software, and Decision Frameworks* (2024), IEEE Computer Society, pp. 1–11. 2

[SHV21] SIDDIQUI F., HÖLLT T., VILANOVA A.: A progressive approach for uncertainty visualization in diffusion tensor imaging. *Computer Graphics Forum 40*, 3 (2021), 411–422. tex.eprint: https://onlinelibrary.wiley.com/doi/pdf/10.1111/cgf.14317. doi:https://doi.org/10.1111/cgf.14317. 2

[SSSSW13] SCHULTZ T., SCHLAFFKE L., SCHÖLKOPF B., SCHMIDT-WILCKE T.: HiFiVE: A hilbert space embedding of fiber variability estimates for uncertainty modeling and visualization. *Computer Graphics Forum 32* (June 2013). doi:10.1111/cgf.12099. 3

[SVBK13] SCHULTZ T., VILANOVA A., BRECHEISEN R., KINDLMANN G.: Fuzzy Fibers: Uncertainty in dMRI Tractography, July 2013. arXiv:1307.3271, doi:10.48550/arXiv.1307.3271. 2

[TCC07] TOURNIER J.-D., CALAMANTE F., CONNELLY A.: Robust determination of the fibre orientation distribution in diffusion MRI: non-negativity constrained super-resolved spherical deconvolution. *Neuroimage 35*, 4 (2007), 1459–1472. Publisher: Elsevier. URL: https://www.sciencedirect.com/science/article/pii/S1053811907001243. 3

[TCGC04] TOURNIER J.-D., CALAMANTE F., GADIAN D. G., CONNELLY A.: Direct estimation of the fiber orientation density function from diffusion-weighted MRI data using spherical deconvolution. *Neuroimage 23*, 3 (2004), 1176–1185. Publisher: Elsevier. URL: https://www.sciencedirect.com/science/article/pii/S1053811904004100. 2, 3

[TCR*13] TOURNIER J., COUNSELL S., RAFFELT D., TUSOR N., NONGENA P., EDWARDS D., HAJNAL J. V., CONNELLY A.: High b-value hardi analysis in neonates scanned at term-equivalent age reveals correlation between apparent white matter fibre density and immaturity at birth. *Proceedings of the International Society for Magn Res Med, Salt Lake City, UT, USA* (2013). 2

[TRW*02] TUCH D. S., REESE T. G., WIEGELL M. R., MAKRIS N., BELLIVEAU J. W., WEDEEN V. J.: High angular resolution diffusion imaging reveals intravoxel white matter fiber heterogeneity. *Magnetic Resonance in Medicine 48*, 4 (Oct. 2002), 577–582. doi:10.1002/mrm.10268. 2, 7

[vAPP*11] VAN ALMSICK M., PEETERS T. H., PRCKOVSKA V., VILANOVA A., TER HAAR ROMENY B.: GPU-Based Ray-Casting of Spherical Functions Applied to High Angular Resolution Diffusion Imaging. *IEEE Transactions on Visualization and Computer Graphics 17*, 5 (May 2011), 612–625. Conference Name: IEEE Transactions on Visualization and Computer Graphics. doi:10.1109/TVCG.2010.61. 2, 3

[WJA*17] WALD I., JOHNSON GP., AMSTUTZ J., BROWNLEE C., KNOLL A., JEFFERS J., GÜNTHER J., NAVRATIL P.: OSPRay - A CPU Ray Tracing Framework for Scientific Visualization. *IEEE Transactions on Visualization and Computer Graphics 23*, 1 (Jan. 2017), 931–940. doi:10.1109/TVCG.2016.2599041. 7

[WSSS14] WIENS V., SCHLAFFKE L., SCHMIDT-WILCKE T., SCHULTZ T.: Visualizing Uncertainty in HARDI Tractography Using Superquadric Streamtubes. *EuroVis - Short Papers* (2014), 5 pages. doi:10.2312/EUROVISSHORT.20141154. 2

[ZCH*17] ZHANG C., CAAN M., HÖLLT T., EISEMANN E., VILANOVA A.: Overview + detail visualization for ensembles of diffusion tensors. *Computer Graphics Forum 36*, 3 (2017), 121–132. doi:https://doi.org/10.1111/cgf.13173. 3

[ZSL*16] ZHANG C., SCHULTZ T., LAWONN K., EISEMANN E., VILANOVA A.: Glyph-Based Comparative Visualization for Diffusion Tensor Fields. *IEEE Transactions on Visualization and Computer Graphics 22*, 1 (Jan. 2016), 797–806. doi:10.1109/TVCG.2015.2467435. 3